ICAS 2020 SHANG HAI
International Council of the Aeronautical Sciences
32nd Congress of the International Council of the Aeronautical Sciences
September 6-10, 2021
Pudong Shangri-La, Shanghai, China

A DESIGN METHOD OF AN AXISYMMETRIC HYPERSONIC INLET INTEGRATED WITH A LONG FOREBODY

Shangcheng Xu, Yi Wang, Zhenguo Wang, Xiaoqiang Fan & Bing Xiong

Science and Technology on Scramjet Laboratory, College of Aerospace Science and Engineering,

National University of Defense Technology, Changsha, Hunan 410073, China

Abstract

To realize the axisymmetric hypersonic inlet design integrated with a long forebody, a conception of streamline-on-lip design is proposed in this paper. An optimization method based on the evolutionary algorithm is applied to acquire satisfactory flowfields. The inlet mass flow as well as the volume of forebody are both considered in the flowfield optimization. Then, the streamline-dependent area and the forebody configuration are obtained utilizing the Machline tracing technique in the optimized flowfield. In the design of inlet compression wall, a limiting wall is proposed and solved by the method of characteristics to reach the maximum compression for the airflow without affecting the inlet mass flow. Results indicate that the full airflow capture can be achieved when the inlet compression wall is not higher than the limiting wall. Finally, two inlets with different compression walls are designed integrated with the obtained long forebody. It is found that an inlet with a large internal contraction ratio usually shows a high total pressure recovery but a poor starting performance. Therefore, the quality of the captured airflow and the starting ability should be balanced in the current inlet design.

Keywords: Integrated forebody/inlet; Streamline-on-lip; Limiting wall; Inlet mass flow

1. Introduction

Scramjet propulsion remains of interest for hypersonic flight with efficiency being the motivating factor [1]. As one of the most important elements, inlet is desired to provide a certain amount of high-performance airflow to the combustor [2]. Besides, forebody undertakes a part of external compression for the incoming airflow in hypersonic condition, which means that forebody also plays a key role in the performances of the propulsion system. Considering the operation process of the hypersonic inlet system, it is necessary to develop design approaches for forebody/inlet integration to improve scramjet performances. However, this task faces great challenges due to complex flow coupling, strong geometrical constraints and strict aerodynamic requirements. So far, research on forebody/inlet integration has attracted considerable public attention and a large number of meaningful studies have been carried out [3-6].

Smart [7, 8] designed a rectangular-to-elliptical shape transition inlet, and integrated this type of inlet with a planar vehicle and a conical vehicle, respectively. The key of this method was to generate a capture shape that integrated with the desired vehicle shape. Li [9] addressed an integration methodology for a waverider-derived hypersonic inlet and a vehicle forebody via a reverse design method. By constructing a three-dimensional shock wave surface which consisted of internal/planar/external parts with continuous local curvature center, the configuration of a hypersonic waverider forebody integrated with an inward turning inlet was obtained. Ding [10] proposed an inlet/airframe integration approach for a waverider that the forebody, the engine cowl and the wings all rode on a bow shock wave by the reverse design method. Numerical results showed that the integrated waverider had a high lift-to-drag ratio and an ideal pre-compression surface for inlet. From the preceding literature survey, the reverse design method was widely performed in inlet/forebody integration [11,12]. In general, a three-dimensional shock wave was constructed to realize the design of shock-on-lip (SOL), indicating that the shock wave generated by the forebody perfectly impinged on the cowl lip, and also the airflow compressed by the

forebody were captured by the inlet without any additional drag. Then, the flowfield and the corresponding wall configuration were solved by the reverse solution methods, such as the method of characteristics (MOC) and the method of Taylor-Maccoll.

With the development of hypersonic flight technique, multiple constraints and excellent performances are required in forebody/inlet design [13, 14]. Considering the practical application, forebody is increasingly required to load more devices. To satisfy loading demand, a long and thick forebody should be designed and the inlet should be installed at the body of the vehicle to provide necessary space. Results show that a large volume can be obtained utilizing this inlet layout compared with the inlet installed at head or chin. However, it should be noted that the integrated design of an inlet with a long forebody was extremely difficult due to the thick boundary layer at the inlet entrance and the multiple geometric and aerodynamic constraints.

This study focuses on the design of an axisymmetric hypersonic inlet integrated with a long forebody. A novel conception of streamline-on-lip (SLOL) condition is proposed to realize the corresponding flowfield. An optimization method is employed in this flowfield solution considering forebody volume and inlet mass flow. Then the streamline-dependent area and the forebody configuration are obtained by the Machline tracing technique in the optimized flowfield. In the inlet compression wall design, a limiting wall is designed ensuring that the inlet mass capture is not affected by the compression wall. Finally, the forebody/inlet configurations are designed based on the SLOL condition and the aerodynamic performances are numerically investigated.

2. Design method of an axisymmetric inlet integrated with a long forebody

2.1 Sketch of the SLOL design

At first, a typical axisymmetric inlet layout using the SOL condition is illustrated in Figure 1, where x presents the streamwise axis and r is the radial axis. A forebody shock wave is arranged from the conical tip A to the cowl lip C. It is noted that the forebody shock wave impinges on the cowl lip and all the airflow compressed by the shock is captured, indicating that the shock-on-lip condition is realized. The captured airflow is just the flow within the circle with the radius $r_{C'}$ in the freestream field when the SOL condition is met. It means that accurate control of the inlet mass flow can be easily achieved by adjusting the value of $r_{C'}$. In this paper, the circle in the freestream field is named as captured circle. Additionally, the radius of the captured circle $r_{C'}$ can be solved by Eq. (1), where inlet mass flow $\dot{m}$ as well as the incoming airflow parameters of density ρ_∞ and velocity v_∞ are given.

$$r_{C'} = \sqrt{\frac{\dot{m}}{\rho_\infty v_\infty \pi}} \tag{1}$$

In the integrated forebody/inlet design, the total contraction ratio (CR_t) and the internal contraction ratio (CR_{in}) are both essential parameters, which should be given based on the inlet aerodynamic performances and the starting requirements. For a typical axisymmetric hypersonic forebody/inlet using SOL condition, CR_t and CR_{in} can be defined by Eq.(2) and Eq.(3), respectively.

$$CR_t = r_{C'}^2 \Big/ (r_E^2 - r_D^2) \tag{2}$$

$$CR_{in} = (r_C + r_F)\sqrt{(r_C - r_F)^2 + (x_C - x_F)^2} \Big/ (r_E^2 - r_D^2) \tag{3}$$

Figure 1 – Axisymmetric hypersonic inlet utilizing the SOL condition.

To load necessary devices, the forebody should be designed large and thick enough. As a result, the forebody shock should be arranged away from the cowl, which is completely different from the conventional SOL design. In this paper, a novel conception of SLOL is proposed to realize the inlet design integrated with a large-volume forebody. To illustrate the conception, Figure 2 schematically shows the forebody/inlet configuration and the corresponding flowfield structure. It is worth noting that although there is no obvious bound between the forebody and the inlet with the improvement of

the integration level, the configurations of the forebody and the inlet are still divided by point B to describe the flow process clearly. The forebody is quite long and thick to provide necessary space for the loading. The annular inlet is installed on the body. The configuration of the cowl are given according to the vehicle overall design. Moreover, the design flight conditions are as follow, a flight Mach number of 5.4 and a flight height of 26 km with the angle of attack of 0°.

The airflow is compressed by a forebody shock wave at first, and then slightly expended in the long forebody region. Subsequently, the flow is re-compressed by the inlet external compression wall after point *B*. Eventually, inlet captures the airflow below the marked streamline and further compresses it in the internal contraction region. Compared with the inlet designed by SOL condition, the most striking difference is that the forebody shock is no longer intersecting the cowl lip. It should be pointed out that the spillage above the cowl lip inevitably occurs, causing the decline of inlet flow capture ability and the increase of the additional drag. Besides, more low-energy airflow of the boundary layer enters the inlet, leading to the decrease of airflow quality. It implies that in order to satisfy loading demand, some losses in inlet aerodynamic performances are unavoidable. Therefore, it is difficult to realize the inlet design integrated with a long forebody while meeting all aerodynamic requirements.

As seen in Figure 2, the inlet captured region is also a circle in the freestream field but with the radius $r_{S'}$. As a result, the streamline traced from point *S* to the cowl lip *C* is named as the captured streamline. The radius of the captured circle can be calculated by Eq. (1). The total contraction ratio defined by Eq. (4) is called nominal total contraction ratio, which is similar with that of the SOL flowfield. Actually, the inlet can only capture the airflow within the captured circle with the radius $r_{S'}$. Therefore, $CR_{t,real}$ is defined as the ratio of the captured circle area to the throat area. For the researched inlet, $CR_{t,\ nominal}$ and $CR_{t,\ real}$ are 4.20 and 2.55, respectively. Besides, the definition of CR_{in} is the same with that of the inlet designed by the SOL condition, as expressed in Eq. (3).

$$CR_{t,nominal} = r_{C'}^{\ 2} \Big/ r_E^{\ 2} - r_D^{\ 2} \tag{4}$$

$$CR_{t,real} = r_{S'}^{\ 2} \Big/ r_E^{\ 2} - r_D^{\ 2} \tag{5}$$

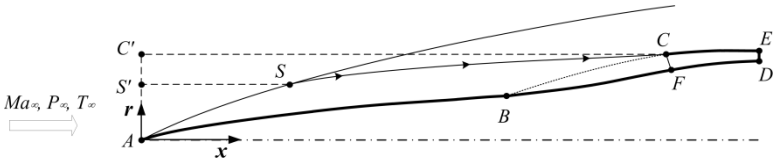

Figure 2 – Axisymmetric inlet integrated with a long forebody utilizing the SLOL condition.

2.2 Solution of forebody flowfields using an optimization method

Considering the difficulty in the SLOL condition solution, parametric optimization is employed to solve the flowfield. Feasible flowfields can be obtained by the optimization algorithm instead of repeated attempts by designer. Besides, the flowfield is optimized in viscid condition, which means that the effect of boundary layer is considered in inlet design.

2.2.1 Parameterization of the forebody wall

The wall of the axisymmetric forebody is parameterized by a quasi-uniform B-spline (QUBS) curve [15]. As illustrated in Figure 3, the curve is controlled by four points, in which point *A* is fixed and the other three green points are flexible in the radial direction. The location of the four points in *x*-axis is shown in the first row of Table 1. It is noted that the parameterized wall is designed longer than the actual forebody to get the positional relation between the captured streamline and the cowl lip. In fact, only the front part of the parameterized curve is utilized as the forebody wall. In the next row, the ranges of these points in *r*-axis are set in view of the flexibility of parameterized wall as well as the optimization efficiency. The radial values of these three flexible points are employed as the optimization variables. Various forebody configurations can be obtained by adjusting the values of variables.

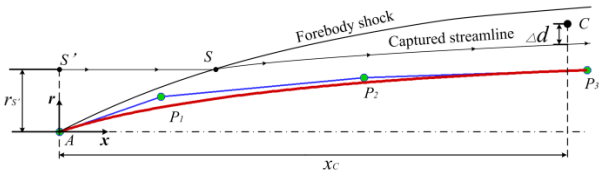

Figure 3 – Parametric generation of the forebody wall and its corresponding flow structure.

Table. 1 Values in *x*-axis and the ranges in *r*-axis of the four controllable points.

Control point	*A*	P_1	P_2	P_3
x / m	0	1	2	2.6
r / m	0	[0.05,0.15]	[0.15,0.25]	[0.25,0.35]

2.2.2 Optimization problem

The most prominent feature of the SLOL condition is that the captured streamline intersects the cowl lip. To obtain the flow structure, the distance $|\Delta d|$ from the captured streamline to the cowl lip in the radial direction (illustrated in Figure 3) should be sufficiently small. In the current optimization process, the flowfield can be regarded as a feasible one and the corresponding inlet can realize full mass capture when it meets the constraint of $|\Delta d|/r_C<0.1\%$. Results indicate that it is enough for a flowfield to meet inlet mass flow demand with this constraint. Besides, the volume of forebody *V* should be large enough to load more devices. In conclusion, the optimization problem can be defined by Eq.(6).

$$\begin{aligned} &\text{Objective: } \min(|\Delta d|/r_C, -V)^{\mathrm{T}} \\ &\text{Subject to: } |\Delta d|/ r_C <0.1\% \end{aligned} \tag{6}$$

To solve the optimization problem, an optimization loop is established. The specific steps in the loop are described as follows:

1) Getting a group of variables by optimization algorithm and parameterizing forebody wall by 3rd QUBS.

2) Generating Grid, simulating the flowfield in viscid condition and tracing the captured streamline.

3) Judging the goals of $|\Delta d|/r_C$ and *V*, starting the next loop.

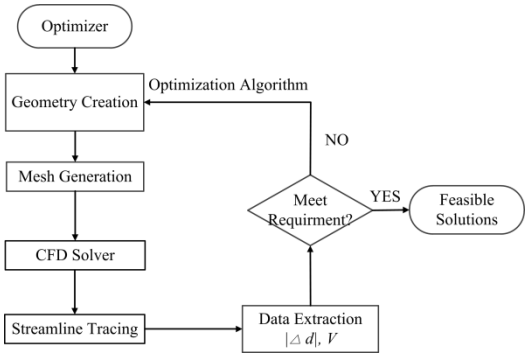

Figure 4 – Diagram of the optimization loop.

2.2.3 Solution of the streamline-dependent area using the reverse Machline tracing

Figure 5 reveals the dependent area and the influence area of a gas parcel in supersonic/hypersonic flowfield. δ represents the flow angle of the gas parcel. λ_1, λ_2 are the left and right Mach angles respectively, which are defined by Eq.(7). According to the theory of MOC, the turbulence of a gas parcel can spread within the influence area outlined by the left and right Machlines. Also, the aerodynamic parameters of a gas parcel are determined by the airflow in the dependent area outlined by the left and right Machlines of two neighboring upstream gas parcels [16].

$$\begin{cases} \lambda_1 = \delta + a\sin(1/Ma) \\ \lambda_2 = \delta - a\sin(1/Ma) \end{cases} \tag{7}$$

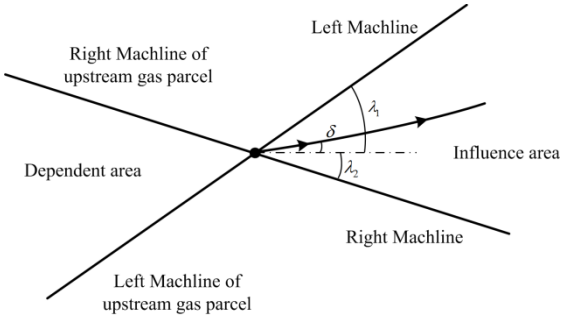

Figure 5 – Illustration of dependent area and influence area of a gas parcel in supersonic/hypersonic flowfield.

In the SOL design, the shape of forebody shock wave is only influenced by the forebody *AB* because the shock is located in the influence area of forebody. As a result, the zone *ABC* is called shock-dependent area. In the SLOL design, the captured streamline is in the influence area of the forebody *AB*. Also, the captured streamline will not be affected only if the forebody *AB* does not change. Accordingly, the region of *ASCB* is defined as the streamline-dependent area.

To obtain the region of the streamline-dependent area *ASCB*, the location of point *B* should be solved. Since the left Machline generated by point *B* just impinges on the cowl lip, a reverse left Mach wave of *CB* can be traced from the cowl lip to the parameterized wall in the optimized flowfield. The reverse Machline tracing technique [16], which is similar with the streamline tracing technique, using a tracing angle λ, can be utilized to trace the left Machline *CB*.

Base on the theory of MOC, the shape of the captured streamline will not be changed with a certain forebody configuration. Moreover, the traced left Machline *CB* is the exit line of the streamline-dependent flowfield as well as the entrance line of the inlet flowfield. Thus, the inlet can be designed using the input condition of *CB* directly, which provides a possibility for the integrated design of forebody/inlet.

2.3 Solution and validation of the limiting wall in the inlet compression wall design

As known, MOC is only applicable in the flowfield where every characteristic line does not intersect with each other. However, if the inlet compression wall is too high, the Mach waves produced by the compression wall will intersect the streamline-dependent area. As a result, the captured streamline will be deflected by excessive compression, leading to the insufficiency of inlet mass flow. This phenomenon will be discussed later. Therefore, it is essential to obtain an special inlet flowfield that all generated Machlines intersect the cowl lip to provide guidance for designing the inlet compression wall (illustrated in Figure 6). In this flowfield, the inlet achieves the largest external compression without affecting the streamline-dependent flowfield. The corresponding compression wall is named as limiting wall. As long as the inlet compression wall is not higher than the limiting wall, the inlet will achieve full mass capture.

In the solution of the limiting wall and its corresponding flowfield, the exit line *CB* of the streamline-dependent area is set as the first compression wave (input condition). MOC is utilized to solve a series of unit processes and obtain a compression wave generated by the compression wall. Then, the bisection method is employed to adjust the wall static pressure until the compression wave intersect the cowl lip. Subsequently, the following compression waves can be acquired by repeating the solving process. Finally, the limiting wall and its corresponding flowfield are obtained.

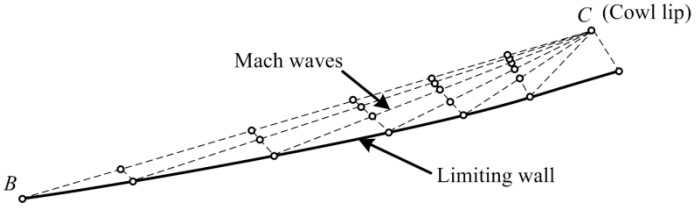

Figure 6 – Solution of the limiting wall using the MOC and the bisection method.

In order to validate the effect of limiting wall on the control of the inlet mass flow, three inlets with different compression wall are designed. The geometrical configuration of the three models are

illustrated in Figure 7. The shapes of the forebody and the cowl of the three models are identical, but there exist some differences in the inlet compression wall. For case A2, the compression wall is just the limiting wall. By contrast, case A1 employs the lower compression wall while case A3 adopts the higher compression wall.

The three models are calculated by the Euler equations in inviscid condition using the density-based implicit solver. As shown in Figure 7, the pressure distributions along the forebody are identical while significant difference occurs in the inlet compression region. Results show that the wall pressure slowly increases for case A1 while it witnesses a sharp rise in case A3. For case A2 with the limiting wall, the curve in the inlet compression region grows slowly at first and then fast. After experiencing pressure drops, three curves all increase rapidly at the inlet entrance caused by the interactions of the cowl shock and boundary layer at compression side.

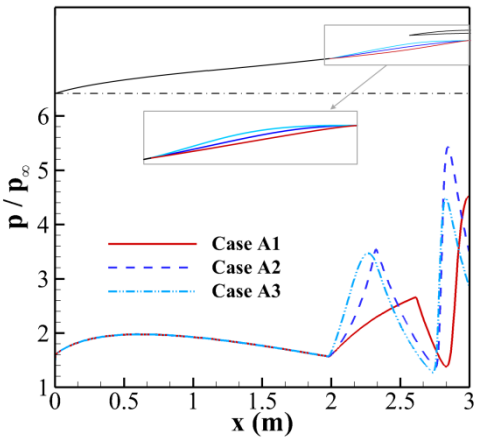

Figure 7 – Geometrical profiles and the pressure distributions of the three models with different inlet compression walls.

The mass flow ratio of case A1 and case A2 reach up to 0.993 and 0.989, respectively, but it is only 0.861 for case A3. The Mach number distributions is presented in Figure 8 to reveal the mechanism of the difference in inlet mass flow. The compression waves produced by the inlet compression wall of case A1 are basically uniform and weak, the first compression wave intersects the cowl lip, and a series of downstream compression waves enter the internal contraction region without distinct convergence. As a result, the captured streamline (the white lines in Figure 8) is not affected by the compression waves. In b), the compression waves of case A2 all gather at the cowl lip, and the captured streamline also impinges on the cowl lip. It is found that the flow structure of case A2 is similar with the flowfield illustrated in Figure 6, which validates the precision of MOC in the limiting wall solution. By contrast, when the compression wall is higher than the limiting wall, as shown in c), the compression waves converge before the cowl lip along the flow direction. As a consequence, the captured streamline is forced to deflect, causing an additional spillage above the cowl lip. That is the reason why the inlet mass flow of case A3 is obviously low. Therefore, as long as the inlet compression wall is not higher than the limiting wall, the captured streamline will not be affected by the compression waves, and thus inlet mass flow will remain unchanged.

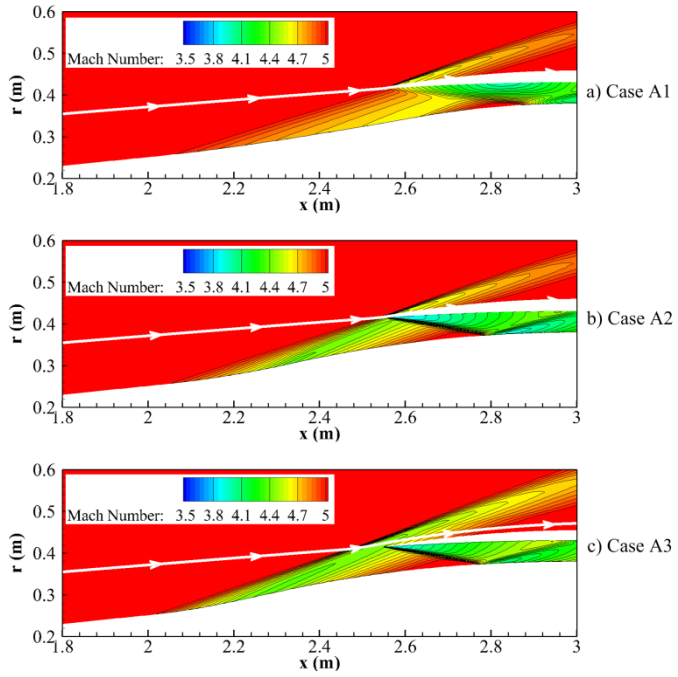

Figure 8 – Mach number distributions of the three models with different compression walls.

3. Numerical method

In the optimization of the forebody flowfield and the research on the aerodynamic performances of the integrated inlet/forebody, the two-dimensional Reynolds-averaged Navier-stokes (RANS) equations are solved. The SST k-ω, as a turbulent model, is utilized to simulate viscid airflow. The air is assumed to be an ideal gas with the viscosity modeled according to the Sutherland law. Due to the axial symmetry of the configuration, the two-dimensional flowfield is required to be solved in the current simulation.

Figure 9 show the structured grids and the boundary conditions employed in the forebody flowfield and the flowfield of the integrated forebody/inlet, respectively. The grid of the forebody flowfield is generated automatically in the optimization loop. The grid size of the forebody flowfield is setting to 300×80 via a grid independence study. In b), the grid points at the inlet entrance and the internal contraction region are refined to accurately calculate the complex flow structures, such as shock wave/boundary layer interactions, shock/shock interactions. The number of grid cells of this flowfield is 42,500. Boundary layer grids are generated in both flowfields to accurately simulate the boundary layer airflow, which results in a suitable y+ value (y+<0.3) for the main portion of the wall flow region. Besides, The pressure far field is assigned as the boundary condition of inflow 1 and inflow 2, and the pressure outlet applied at outflow 1, outflow 2 and outflow 3. No-slip boundary condition is enforced at the wall and the cowl.

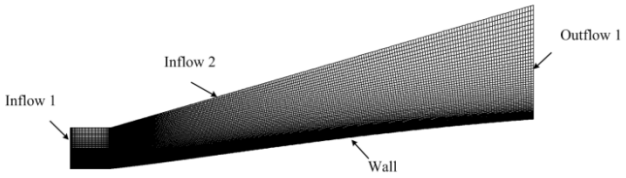

a) Grid of the forebody flowfield applied in the optimization process

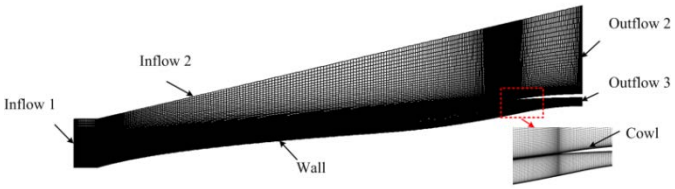

b) Grid of the integrated forebody/inlet flowfield.

Figure 9 –Diagram of grids and boundary conditions employed in the computation region

Moreover, the reverse design method of MOC is imposed on the limiting wall and its corresponding flowfield solutions, and a density-based implicit solver using the Euler equations is applied to validate the precision of MOC.

4. Results and discussion

4.1 Optimization results of the forebody flowfield

NSGA-II [17], one of the most popular multi-objective optimization algorithms, is performed to solve the forebody optimization problem. The population size and the number of generation are set to 20 and 30, respectively. Figure 10 displays the iteration histories of $|\Delta d|/r_C$ and V in the optimization process. It can be seen that $|\Delta d|/r_C$ gradually falls into the target range of $|\Delta d|/ r_C$ <0.1%, implying that the captured streamline is closer to the cowl lip and growing number of feasible flowfields are obtained. Besides, V is gradually converged after about 150 steps.

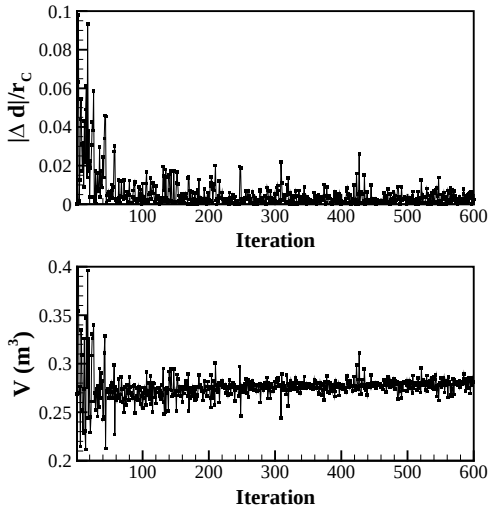

Figure 10 - Iteration histories of $|\Delta d|/r_C$ and V in the optimization process.

Finally, 142 samples are satisfied with the constraint function and become feasible flowfields. Figure 11 shows the distribution of the feasible solutions in $|\Delta d|/r_C$ -V pairs. The smaller the $|\Delta d|/r_C$ is, the better the airflow capture performance is. Also, the larger the V is, the larger the forebody volume is. The final flowfield should be chosen based on the practical application in view of the inlet mass flow and the loading demand of vehicle. In this work, the sample marked by the red circle is selected as the final forebody flowfield. $|\Delta d|/r_C$ of this flowfield is only 0.00002, indicating that the mass flow ratio completely approaches to the design goal. Besides, V of the forebody reaches up to 0.278, achieving a high level of loading capacity among all feasible samples.

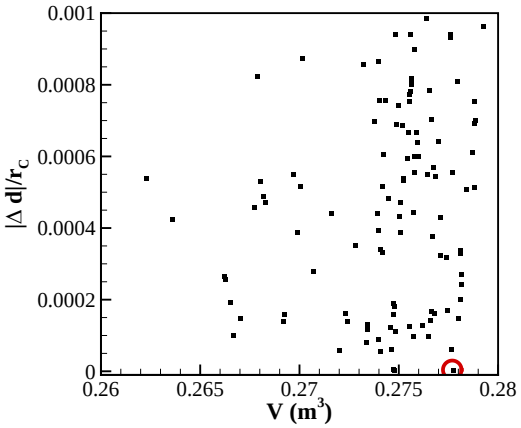

Figure 11 – Distribution of the feasible solutions in $|\Delta d|/r_C$-V pairs.

The wall configuration as well as the Mach number contour of the selected forebody flowfield is displayed in Figure 12. A large conical angle is formed at the tip, and then the forebody wall gradually rises. Correspondingly, a strong curved forebody shock wave is generated at the tip and

then the shock wave gradually becomes weak due to a series of expansion waves. Moreover, a growing boundary layer is formed near the wall because of the viscosity. The captured streamline traced from the incoming airflow just impinges on the cowl lip, indicating that the SLOL condition is achieved. Then, the reverse Machline tracing technique is applied in the flowfield to solve the streamline-dependent area. As shown, a left Machline *CB* is traced from the cowl lip to the forebody wall, thus, the forebody configuration *AB* and the streamline-dependent area are obtained.

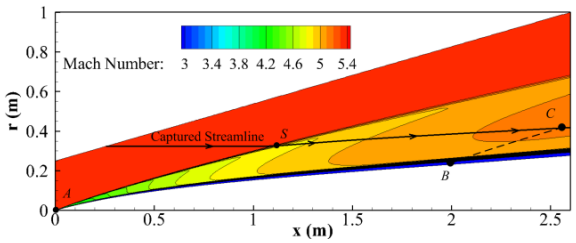

Figure 12 – Mach number contour of the optimized forebody flowfield.

4.2 Design and analysis of integrated forebody/inlet with various geometric profiles

In general, inlet should be designed satisfying various aerodynamic requirements. Firstly, inlet should capture required airflow and a high mass flow ratio is necessary at the design point. Besides, the total pressure recovery coefficient which represents the quality of the captured airflow should be high enough. Moreover, for a well-designed hypersonic inlet, it should operate in the started mode [18-20]. According to the Kantrowitz limit and the isentropic limit, the start ability of an inlet depends on the local Mach number and internal contraction ratio [21,22]. An inlet with a small internal contraction ratio tends to start at a low Mach number. Moreover, other performances, such as compression efficiency, flow distortion, drag, and so on, should also be considered. In this section, two forebody/inlet configurations are designed based on the SLOL condition and their aerodynamic performances are numerically investigated.

In the current forebody/inlet design, the wall of the obtained streamline-dependent flowfield is directly utilized as the forebody wall. The inlet is designed by employing the exit line of the streamline-dependent flowfield as the input condition, ensuring the smooth connection between the forebody wall and the inlet compression wall. Moreover, the principle of the limiting wall is performed in the compression wall design to obtain the aimed inlet mass flow. Figure 13 shows the geometrical configurations of the two cases (denoted case B1 and case B2, respectively). The forebody walls of both cases are completely the same, and the compression walls of the two cases are both lower than the limiting wall. However, obvious difference can be seen in the compression wall, where the compression wall of case B1 is obviously higher than that of case B2. Figure 14 displays the pressure distributions of the two cases. The static pressure of case B1 in the external compression region rises more rapidly than that of case B2. Moreover, the pressure rise in the internal compression region of case B1 is also relatively higher than that of case B2 due to the stronger cowl shock/boundary layer interactions .

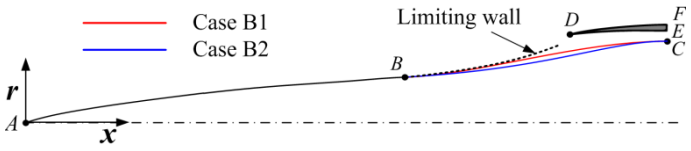

Figure 13 – Two integrated forebody/inlet configurations with different compression walls.

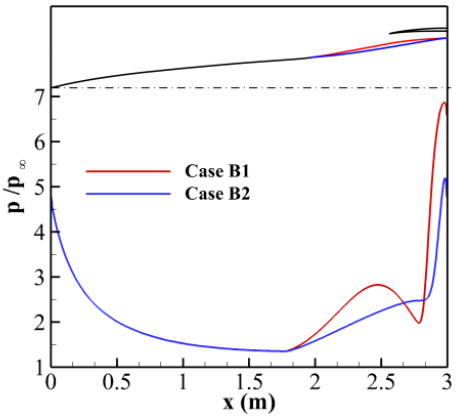

Figure 14 – Static pressure distributions of two designed models.

Table. 2 shows the geometric parameters and the main aerodynamic parameters of the two cases. The $CR_{t,nominal}$ and $CR_{t,real}$ of the two inlets are the same. However, CR_{in} of case B1 is obviously lower than that of case B2 (1.50 in case B1 and 1.84 in case B2, respectively). In view of inlet performances, the two inlets achieve high mass flow ratio, which both satisfy the required mass capture. Moreover, p/p_∞ of case B1 at the throat is slightly higher than that of case B2, but total pressure recovery coefficient of case B1 is 7.51% lower than that of case B2.

Table. 2 Geometric parameters ratios and main aerodynamic parameters at the throat of the two inlets.

Case	$CR_{t,nominal}$	$CR_{t,real}$	CR_{in}	φ	σ	p/p_∞
B1	4.20	2.55	1.50	0.987	0.6671	6.25
B2			1.84	1.01	0.7172	6.13

Figure 15 shows the Mach number contours of the two cases in inlet flowfield. The external compression of case B1 is considerable and a strong cowl shock stands at the inlet entrance due to the large angle between the flow direction of the airflow and the cowl wall. Severe cowl shock/boundary layer interactions occur at the compression side of case B1. By contrast, the compression waves of case B2 are basically well-distributed, and the cowl shock/boundary layer interactions are weak. Therefore, a high total pressure recovery coefficient can be achieved in the flowfield of case B2.

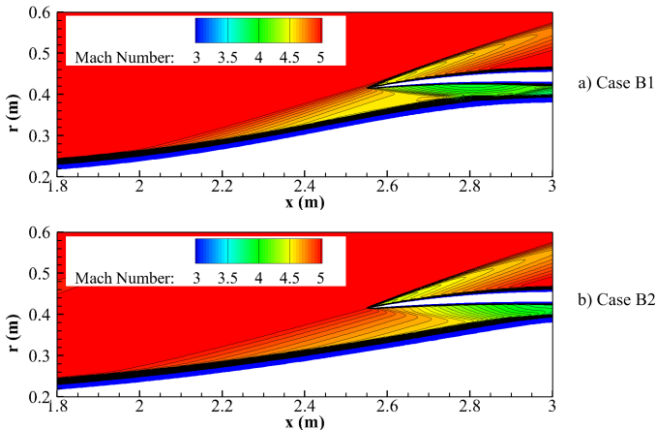

Figure 15 – Mach number contours of the two models in inlet region.

Accelerating self-starting process [23], the variation process that inlet changes from unstart to start with the increase of inflow Mach number, is numerically investigated to evaluate the inlet starting ability. Figure 16 shows the total pressure recovery coefficient distributions of the two inlets during starting process. It is found that the value of case B1 experiences a significant increase at *Ma*=3.1, indicating that case B1 enters start state. Then a similar rise can be seen in case B2 and the inlet

starts at *Ma*=3.6. With the further increase of the inflow Mach number, total pressure recovery coefficients of both inlets decrease gradually due to the stronger shock waves. Obviously, the starting performance of case B1 is better than case B2. However, it can be seen that total pressure recovery of case B2 is higher than that of case B1 at starting state. It indicates that the starting ability and the total pressure recovery performance of the current forebody/inlet are conflicting with each other. Designer should choose suitable inlet compression wall according to the requirement of inlet start and expected total pressure recovery.

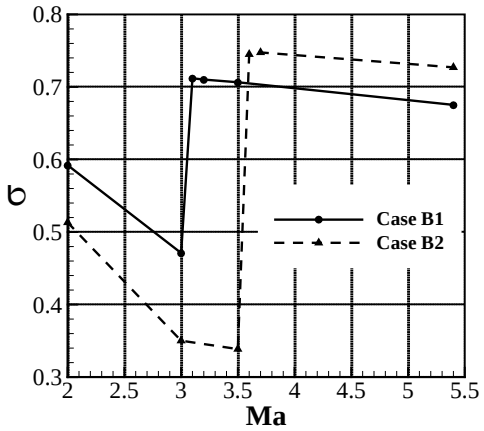

Figure 16 – Total pressure recovery coefficient distributions in the self-starting process of the two cases.

5. Conclusions

To realize the design of an axisymmetric hypersonic inlet integrated with a long forebody, a conception of SLOL is proposed in this paper. An optimization method is carried out to obtain the corresponding flowfields. Then, two integrated forebody/inlet configurations are designed based on the SLOL condition, and their aerodynamic performances are numerically investigated. The conclusions can be drawn as follows,

(1) The forebody flowfield utilizing the SLOL condition is optimized, and 142 feasible flowfields are obtained by the proposed optimization method. Subsequently, the streamline-dependent area is solved by using the reverse Machline tracing technique in the optimized flowfield.

(2) A conception of the limiting wall is proposed and solved by MOC to overcome the difficulty in inlet mass flow control. Results indicate that as long as the inlet compression wall designed is not higher than the limiting wall, inlet mass flow ratio will not be affected.

(3) Two integrated inlet/forebody configurations with different compression wall are designed utilizing the SLOL condition. Result reveals that both inlets can capture required mass flow in viscid condition. Moreover, it is found that the starting ability and the total pressure recovery performance of the current forebody/inlet are conflicting with each other. It suggests that the quality of the captured flow and the starting ability should be balanced in the current inlet design.

Acknowledgements

The authors gratefully acknowledge the support of the Hunan Provincial Innovation Foundation for Postgraduate (Nos. CX20200082).

References

[1] Seddon J, Goldsmith EL. *Intake aerodynamics*. 2nd edition, Ohio: Air Force Institute of Technology; 1999.

[2] Gaiddon A, Knight DD. Multicriteria design optimization of integrated three-dimensional supersonic inlets. *Journal of Propulsion Power*, Vol. 159, No. 3, pp 456-463, 2003.

[3] Tan H J, Chen Z, Li GS. A new concept and preliminary study of variable hypersonic inlet with fixed geometry based on shockwave control. *Science China Technological Sciences*, Vol. 50, pp 644–657, 2007.

[4] Wang JF, Cai JS, Liu CZ, Duan YH, Yu YJ. Aerodynamic configuration integration design of hypersonic cruise

aircraft with inward-turning inlets. *Chinese Journal of Aeronautics*, Vol. 30, No. 4, pp1349-1362, 2017.

[5] Huang GP, Zuo FY, Qiao WY. Design method of internal waverider inlet under non-uniform upstream for inlet/forebody integration. *Aerospace Science Technology*, Vol. 74, pp 112-124, 2018.

[6] Bissinger NC, Blagoveshchensky NA, Gubanov AA, et al. Improvement of forebody/inlet integration for hypersonic vehicle. *Aerospace Science Technology*, Vol. 8, pp 505-514, 1998.

[7] Smart MK. Design of three-dimensional hypersonic inlets with rectangular-to-elliptical shape transition. *Journal of Propulsion Power*, Vol. 15, No. 3, pp 408-416, 1999.

[8] Gollan RJ, Smart MK. Design of modular shape-transition inlets for a conical hypersonic vehicle. *Journal of Propulsion Power*, Vol. 29, No. 4, pp 832-838, 2013.

[9] Li YQ, An P, Pan CJ, Pan JC, Chen RQ, You YC. Integration methodology for waverider-derived hypersonic inlet and vehicle forebody. *AIAA*, 2014, Report No.2014-3229.

[10] Ding F, Liu J, Shen CB, Huang W. Novel inlet-airframe integration methodology for hypersonic waverider vehicles. *Acta Astronautica*, Vol. 111, pp 178-197, 2015.

[11] Zuo FY, Mölder S. Hypersonic wavecatcher intakes and variable-geometry turbine based combined cycle engines. *Progress in Aerospace Sciences*, Vol. 106, pp 108-144, 2019.

[12] Qiao WY, Yu AY, Gao W, Wang WX. Design method with controllable velocity direction at throat for inward-turning inlets, *Chinese Journal of Aeronautics*, Vol. 32, No. 6, pp1403-1415, 2019.

[13] Xiong B, Fan XQ, Wang Y. Deficiencies of streamline tracing techniques for designing hypersonic inlets and potential solutions. *Science China Technological Sciences*, Vol. 63, No. 3, pp 488-495, 2020.

[14] Xiong B, Fan XQ, Wang Y. Parameterization and optimization design of an inward turning inlet. *Acta Astronautica*, Vol. 164, pp 130-141, 2019.

[15] Lee C, Koo D, Zingg D. Comparison of B-spline surface and free-form deformation geometry control for aerodynamic optimization. *AIAA Journal*, Vol. 55, No. 1, pp 228-240, 2017.

[16] Xu SC, Wang Y, Wang ZG, Fan XQ, Zhao XY. Design and analysis of a hypersonic inlet with an integrated bump/forebody. *Chinese Journal of Aeronautics*, Vol. 32, No. 10, pp 2267-2274, 2019.

[17] Deb K, Pratap A, Agarwal S, Meyarivan T. A fast and elitist multi-objective genetic algorithm: NSGA-Ⅱ. *IEEE Transactions on Evolutionary Computation*, Vol. 6, No. 2, pp182-197, 2002.

[18] Bai CY, Li J, Li S, Li SC, Wu ZN. Review of theoretical achievements for starting flow problem for all Mach number. *Chinese Journal of Aeronautics*, Vol. 32, No. 1, pp78-91, 2019.

[19] Billig FS, Baurle RA, Tam CJ. Design and analysis of streamline traced hypersonic inlets. *AIAA*, 1996, Report No. 1996-4974.

[20] Van Wie DM, Kwok F, Walsh R. Starting characteristics of supersonic inlet. *AIAA*, 1996, Report No.1996-2914.

[21] Kantrowitz A, Donaldson C. Preliminary investigation of supersonic diffusers. *NACA*, 1945, Report No. ACR-L5D20.

[22] Kantrowitz A. The formation and stability of normal shock waves in channel flows. *NACA*, 1947, Report No.TN-1225.

[23] Chang JT, Li N, Xu KJ, Bao W, Yu DR. Recent research progress on unstart mechanism, detection and control of hypersonic inlet. *Progress in Areospace Sciences*, Vol. 89, pp 1-22, 2017.

Contact Author Email Address

mailto: wange_nudt@163.com

Copyright Statement